

A tensor network approach for chaotic time series prediction

Rodrigo Martínez-Peña^{1,*} and Román Orús^{1,2,3}

¹Donostia International Physics Center, Paseo Manuel de Lardizabal 4, E-20018 San Sebastián, Spain

²Multiverse Computing, Paseo de Miramón, E-20014 San Sebastián, Spain

³Ikerbasque Foundation for Science, Maria Diaz de Haro 3, E-48013 Bilbao, Spain

*rodrigo.martinez@dipc.org

ABSTRACT

Making accurate predictions of chaotic time series is a complex challenge. Reservoir computing, a neuromorphic-inspired approach, has emerged as a powerful tool for this task. It exploits the memory and nonlinearity of dynamical systems without requiring extensive parameter tuning. However, selecting and optimizing reservoir architectures remains an open problem. Next-generation reservoir computing simplifies this problem by employing nonlinear vector autoregression based on truncated Volterra series, thereby reducing hyperparameter complexity. Nevertheless, the latter suffers from exponential parameter growth in terms of the maximum monomial degree. Tensor networks offer a promising solution to this issue by decomposing multidimensional arrays into low-dimensional structures, thus mitigating the curse of dimensionality. This paper explores the application of a previously proposed tensor network model for predicting chaotic time series, demonstrating its advantages in terms of accuracy and computational efficiency compared to conventional echo state networks. Using a state-of-the-art tensor network approach enables us to bridge the gap between the tensor network and reservoir computing communities, fostering advances in both fields.

Introduction

Chaos is a ubiquitous phenomenon in nature, and it is present in such diverse fields as weather and climate¹, population dynamics², and nonlinear optics³. High sensitivity to initial conditions leads to exponentially growing errors and makes the efficient prediction of chaotic time series a challenging problem. A wide spectrum of data-driven machine learning models can be employed for this task, ranging from recurrent kernel methods^{4,5} to long short-term memory networks⁶ and transformers⁷. A popular approach in this direction is reservoir computing (RC)^{8–12}. Inspired by the field of neuromorphic computing, it exploits the intrinsic memory and nonlinearity of dynamical systems to process temporal information. The most important feature of this technique is that it does not require a fine-tuning of the dynamical system's parameters (usually randomly generated), relying only on the training of an (in most cases linear) output layer. This quick training, together with their universal approximation^{13–16} and embedding^{11,12} properties, makes RC models very attractive for the forecasting of chaotic systems.

Nevertheless, the selection and optimization of reservoirs is an open problem. A very popular approach is the echo state networks (ESNs)^{17–20}, which have demonstrated high performance in empirical studies and are also known for their universal approximation properties^{14–16,21}. However, ESNs require the exploration of several hyperparameters for each task, which increases the complexity for real-world applications. An alternative strategy is the realization of dedicated hardware, which could enable speed gains and power savings with plenty of possible physical substrates^{22–24}. However, although physical RC has the potential for large-scale applications, several challenges prevent its industrial adoption, requiring more research in both theoretical and experimental aspects²⁵.

A third approach is to change the reservoir by a nonlinear vector autoregression, where the state vector consists of a linear combination of delayed input monomials. This idea is known as next-generation reservoir computing (NGRC)²⁶, and is successful in predicting and controlling chaotic systems^{27–30}, reducing the hyperparameter optimization to only two variables, maximum delay and maximum monomial degree. The key feature behind NGRC is that state vectors are truncated versions of the Volterra series, which has universal approximation properties^{31,32}. Still, state-space models given by a truncated Volterra series can be elusive due to the exponential growth of trainable parameters regarding the maximum monomial degree. Hence, there is a strong motivation to solve this curse of dimensionality, finding a promising direction in the field of tensor networks (TNs)^{33–38}.

Tensor networks are techniques based on decomposing multidimensional arrays into a set of lower-dimensional arrays, called core tensors. These core tensors can be efficiently manipulated and stored in memory, having applications in such

diverse fields as quantum mechanics^{39,40}, machine learning^{41–43}, and engineering^{38,44}. This paper illustrates that a TN model can predict chaotic time series better and faster than a conventional ESN model. In particular, we will implement one of the latest models proposed for truncated Volterra series³⁵, which only depends, as in the NGRC case, on the maximum delay and maximum monomial degree. To evaluate the performance of our models, we use the `dysts` database^{7,45}. This library provides a standardized collection of chaotic systems often used to benchmark time series forecasting methods. Our key goal is to bridge the gap between the TNs and RC communities, harnessing the developments of both fields during the last two decades.

The structure of the paper is as follows. The Section Methods introduces the notation, numerical details, and the truncated Volterra series TN implementation of reference 35. The Section Results contains the numerical results of benchmarking the models in terms of performance and computational speed. Finally, the Section Discussion summarizes the main contributions of the paper.

Methods

Tensors

A D th-order tensor $\mathcal{X} \in \mathbb{R}^{I_1 \times \dots \times I_D}$ is a multidimensional array with $D \in \mathbb{N}$ indices; that is, each entry can be written as $\mathcal{X}(i_1, \dots, i_D)$. Most common tensors are scalars ($D = 0$), vectors ($D = 1$), and matrices ($D = 2$), and we will denote them as x , \mathbf{x} , and \mathbf{X} , respectively. D th-order symmetric tensors $\mathcal{X} \in \mathbb{R}^{I \times \dots \times I}$, which are of particular interest for us, are those invariant under index permutation:

$$\mathcal{X}(i_1, \dots, i_D) = \mathcal{X}(\pi(i_1, \dots, i_D)), \quad (1)$$

where $\pi(i_1, \dots, i_D)$ stands for any possible permutation of D indices. We denote by $\text{Sym}_D(\mathbb{R})$ the vector space of symmetric tensors of order D over the reals.

Let us now introduce some important tensor transformations. The reshape operation modifies the order of a tensor such that a D th-order tensor $\mathcal{X} \in \mathbb{R}^{I_1 \times \dots \times I_D}$ is rearranged to form a $\mathcal{Y} \in \mathbb{R}^{J_1 \times \dots \times J_K}$ without changing the total number of entries, that is, $\prod_{d=1}^D I_d = \prod_{k=1}^K J_k$. We denote the operation as $\mathcal{Y} = \text{reshape}(\mathcal{X}, \{J_1, J_2, \dots, J_K\})$. The vectorization is a reshape operation that converts a D th-order tensor $\mathcal{X} \in \mathbb{R}^{I_1 \times \dots \times I_D}$ in a vector $\mathbf{x} \in \mathbb{R}^{\prod_{d=1}^D I_d}$, and we will denote it as $\mathbf{x} = \text{vec}(\mathcal{X})$. The conversion of D indices i_1, \dots, i_D into a multi-index $[i_1 i_2 \dots i_D]$ is defined as

$$[i_1 i_2 \dots i_D] = i_1 + \sum_{d=2}^D (i_d - 1) \prod_{m=1}^{d-1} I_m, \quad (2)$$

such that the entries of a vectorized tensor fulfill

$$\mathcal{X}(i_1, \dots, i_D) = \mathbf{x}([i_1 i_2 \dots i_D]). \quad (3)$$

In this manuscript, we are interested in efficient decompositions of matrices with a curse of dimensionality. A well-established technique for matrix decomposition is low-rank approximation, with singular value decomposition (SVD) being a prominent example⁴⁶. The rank of a matrix, denoted as R , corresponds to the number of its nonzero singular values. By truncating small singular values, we can enhance storage efficiency and computational performance while maintaining an effective approximation of the original matrix⁴⁷. This concept extends beyond matrices to higher-order tensors, giving rise to various tensor decomposition methods, each with distinct characteristics and rank definitions^{48–50}.

In this work, we utilize matrix product operators (MPOs) for matrix decomposition. An MPO, also known as a tensor train matrix, decomposes a matrix with exponential dimensions in a linear sequence of core tensors^{51–53}. Consider a matrix $\mathbf{X} \in \mathbb{R}^{I^D \times J^D}$. We split each row and column into D indices i_1, \dots, i_D and j_1, \dots, j_D , defining the multi-indices $[i_1 i_2 \dots i_D] = i_1 + \sum_{d=2}^D (i_d - 1) I^{d-1}$ and $[j_1 j_2 \dots j_D] = j_1 + \sum_{d=2}^D (j_d - 1) J^{d-1}$, such that \mathbf{X} can be reshaped into a $2D$ th-order tensor $\mathcal{X} \in \mathbb{R}^{I \times \dots \times I \times J \times \dots \times J}$. This tensor can be decomposed as an MPO that consists of D fourth-order tensors $\mathcal{X}^{(d)} \in \mathbb{R}^{R_d \times i_d \times j_d \times R_{d+1}}$, such that each matrix entry can be computed as

$$\mathbf{X}([i_1 \dots i_D], [j_1 \dots j_D]) = \sum_{r_1=1}^{R_1} \dots \sum_{r_D=1}^{R_D} \mathcal{X}^{(1)}(r_1, i_1, j_1, r_2) \mathcal{X}^{(2)}(r_2, i_2, j_2, r_3) \dots \mathcal{X}^{(D)}(r_D, i_D, j_D, r_1), \quad (4)$$

where $R_1 = 1$.

Truncated Volterra series

Let us introduce the truncated Volterra series. Let $M \in \mathbb{N}$ be the maximum delay of the series and $D \in \mathbb{N}$ the maximum order of the monomials. We define each d th-order Volterra series kernel $h_d(m_1, \dots, m_d)$ as a function of the delays m_j for $j = 1, \dots, d$ and $m_j = 0, \dots, M - 1$. Let input and output be bi-infinite discrete-time sequences of the form $\mathbf{u} = (\dots, u(-1), u(0), u(1), \dots) \in \mathbb{R}^{\mathbb{Z}}$ and $\mathbf{y} = (\dots, y(-1), y(0), y(1), \dots) \in \mathbb{R}^{\mathbb{Z}}$ respectively. Then, the single-input single-output truncated series is defined as

$$y(n) = h_0 + \sum_{d=1}^D \sum_{m_1, \dots, m_d=0}^{M-1} h_d(m_1, \dots, m_d) \prod_{j=1}^d u(n - m_j). \quad (5)$$

Now, following e.g., reference 33, we will define the multivariate case in a compact matrix form. Let us define the P -dimensional input and L -dimensional output as

$$\begin{aligned} \mathbf{u}(n) &:= (u_1(n), u_2(n), \dots, u_p(n))^{\top} \in \mathbb{R}^P, \\ \mathbf{y}(n) &:= (y_1(n), y_2(n), \dots, y_p(n))^{\top} \in \mathbb{R}^L, \end{aligned} \quad (6)$$

for all $n \in \mathbb{Z}$. To obtain the truncated Volterra series, one needs to compute all the possible monomials of the input in terms of the hyperparameters M and D . We start by introducing an extended vector of the input as

$$\mathbf{u}_n := (1, \mathbf{u}(n)^{\top}, \dots, \mathbf{u}(n - M + 1)^{\top})^{\top} \in \mathbb{R}^I, \quad (7)$$

with $I := PM + 1$. Then, we define the vector containing all the monomials of the input up to degree D using repeated Kronecker products:

$$\mathbf{u}_n^D := \overbrace{\mathbf{u}_n \otimes \dots \otimes \mathbf{u}_n}^{D \text{ times}} \in \mathbb{R}^{I^D}. \quad (8)$$

The \mathbf{u}_n^D vectors are a vectorization of a symmetric tensor of D indices with I possible values each. This fact will be relevant for the next section. Then, at each time step, the truncated Volterra series is determined by

$$\mathbf{y}(n)^{\top} = (\mathbf{u}_n^D)^{\top} \mathbf{H}, \quad n \in \mathbb{Z}, \quad (9)$$

where \mathbf{H} is the Volterra coefficients matrix with dimension $I^D \times L$. This equation can be extended to include N time steps as follows:

$$\begin{pmatrix} \mathbf{y}(1)^{\top} \\ \vdots \\ \mathbf{y}(N)^{\top} \end{pmatrix} = (\mathbf{u}_1^D \quad \dots \quad \mathbf{u}_N^D)^{\top} \mathbf{H}, \quad (10)$$

or in a more compact form,

$$\mathbf{Y} = \mathbf{U} \mathbf{H}, \quad (11)$$

where matrices \mathbf{Y} and \mathbf{U} have dimensions $N \times L$ and $N \times I^D$ respectively. Since each row of matrix \mathbf{U} is given by the D -times repeated Kronecker product, we can rewrite \mathbf{U} in terms of repeated row-wise Khatri-Rao products⁵⁴. Define the $N \times I$ matrix $\tilde{\mathbf{U}}$ as

$$\tilde{\mathbf{U}} := \begin{pmatrix} \mathbf{u}_1^{\top} \\ \vdots \\ \mathbf{u}_N^{\top} \end{pmatrix}, \quad (12)$$

then \mathbf{U} can be rewritten as

$$\mathbf{U} = \overbrace{\tilde{\mathbf{U}} \odot \dots \odot \tilde{\mathbf{U}}}^{D \text{ times}}, \quad (13)$$

where \odot denotes the row-wise Khatri-Rao product.

Finally, we define the learning problem: Given a finite sequence $\{\mathbf{u}(n), \mathbf{y}(n)\}_{n=1}^N$ of training data, a maximum monomial degree D and a maximum delay M , find the unknown \mathbf{H} matrix that better fits the training dataset. Since Eq. (11) is a linear system, the naive solution would be to go straightforward for the least squares solution, given by

$$\mathbf{H} = \mathbf{U}^+ \mathbf{Y}, \quad (14)$$

with \mathbf{U}^+ being the Moore–Penrose pseudoinverse. However, the exponential scaling in terms of the hyperparameter D makes this computation hard in general. Some solutions to solve this curse of dimensionality are: PARAFAC^{36–38,55,56}, MPOs optimized with DMRG³³, MPOs with extra structure using a Bayesian framework⁵⁷, and MPOs enforcing symmetry in the tensors’ solution^{34,35}. We will focus on the latter case³⁵, since it is the simplest algorithm in terms of the number of hyperparameters and it offers high speed of training. Nevertheless, our source code also includes the implementation of references 33, 34, which can be of interest to some readers.

MPOs enforcing symmetry

Each row of the matrix \mathbf{U} in Eq. (11) is the vectorization of a symmetric tensor. This means that the vectors \mathbf{u}_n^D contain repeated entries due to the symmetry introduced by the Kronecker products. This symmetry bounds the rank of \mathbf{U} , as shown in Lemma 4.2 of 33, namely:

$$\text{rank}(\mathbf{U}) \leq R = \binom{PM+D}{PM}. \quad (15)$$

where R is the maximum number of independent coefficients (or monomials) of the truncated Volterra series.

Since matrix \mathbf{U} has dimensions $N \times I^D$, it is a rank-deficient matrix and the normal equation

$$\mathbf{U}^\top \mathbf{U} \mathbf{H} = \mathbf{U}^\top \mathbf{Y} \quad (16)$$

for the least squares problem of Eq. (11) has an infinite number of solutions, independently of the number of samples N . In Proposition 4.2 of 33, it was shown that under the assumption of persistently exciting input, that is, $\text{rank}(\mathbf{U}) = R$ ($N \geq R$), each column of the unique minimal-norm solution for \mathbf{H} is the vectorization of a D -dimensional symmetric tensor. We show in the Appendix that this result is independent of the rank of \mathbf{U} . Therefore, finding the minimum-norm solution of Eq. (11) is equivalent to enforcing symmetry on the columns of \mathbf{H} .

The minimum-norm solution is computed using the pseudoinverse, which is obtained through SVD. Assume that $N > R$, the SVD of matrix \mathbf{U} is

$$\mathbf{U} = \mathbf{Q} \begin{pmatrix} \mathbf{S} & 0 \\ 0 & 0 \end{pmatrix} \mathbf{V}^\top = (\mathbf{Q}_1 \quad \mathbf{Q}_2) \begin{pmatrix} \mathbf{S} & 0 \\ 0 & 0 \end{pmatrix} \begin{pmatrix} \mathbf{V}_1^\top \\ \mathbf{V}_2^\top \end{pmatrix} = \mathbf{Q}_1 \mathbf{S} \mathbf{V}_1^\top, \quad (17)$$

where $\mathbf{Q} \in \mathbb{R}^{N \times N}$, $\mathbf{V} \in \mathbb{R}^{I^D \times I^D}$, $\mathbf{Q}_1 \in \mathbb{R}^{N \times R}$, $\mathbf{V}_1 \in \mathbb{R}^{I^D \times R}$ are orthogonal matrices and $\mathbf{S} \in \mathbb{R}^{R \times R}$ is the diagonal matrix of non-zero singular values. Finally, the symmetric Volterra kernel coefficients can be obtained as

$$\mathbf{H} = \mathbf{V}_1 \mathbf{S}^{-1} \mathbf{Q}_1^\top \mathbf{Y}. \quad (18)$$

Computing the SVD of \mathbf{U} is computationally inefficient due to the exponential number of columns in terms of D . However, this problem can be overcome if MPOs are introduced to decompose both \mathbf{U} and \mathbf{H} in Eq. (11). The construction of these MPOs was originally proposed in 34, where repeated Khatri–Rao products together with truncated SVDs were required. However, reference 35 proposes to replace this construction with an exact representation that does not involve computations and only instances of matrix $\tilde{\mathbf{U}}$ need to be stored. We refer to 35 for further details of this construction.

ESN benchmark

Echo state networks (ESNs) were introduced two decades ago as an alternative to the more traditional recurrent neural networks (RNNs)⁵⁸. ESNs have become one of the most popular RC families due to their simplicity, easy training, and competitive performance compared with RNNs. In this work, we use ESNs as a benchmark to compare with the performance and training time of the TN model.

Different versions of the ESN model were tested, but we will only show the leaky version, which finds a compromise between performance and running time for hyperparameter optimization (both the ESN without leaky rate and the ESN with offset can be found in the source code). Let us define $\mathbf{x}(n) \in \mathbb{R}^{N_r}$ as the state vector for N_r neurons at time step $n \in \mathbb{Z}$, its dynamics is given by

$$\mathbf{x}(n) = (1 - \varepsilon) \mathbf{x}(n-1) + \varepsilon \tanh(\mathbf{W} \mathbf{x}(n-1) + g \mathbf{v} \mathbf{u}(n)), \quad (19)$$

where $W \in \mathbb{R}^{N_r \times N_r}$ is the connectivity matrix, $\mathbf{v} \in \mathbb{R}^{N_r \times P}$ is the connectivity input vector and $\tanh(\cdot)$ is applied element-wise, $g \in \mathbb{R}^+$ is the input strength, and $\varepsilon \in [0, 1]$ is the leak rate. The elements of arrays W and \mathbf{v} are randomly generated from a uniform distribution $[-1, 1]$. The spectral radius ρ of the matrix W will be controlled as a hyperparameter as well.

The output layer $\mathbf{y}(n) \in \mathbb{R}^L$ of the ESN model is constructed as follows:

$$\mathbf{y}(n)^\top = \mathbf{x}(n)^\top W^{\text{out}} + \mathbf{b}^\top, \quad (20)$$

where $W^{\text{out}} \in \mathbb{R}^{N_r \times L}$ is the output weight matrix and $\mathbf{b} \in \mathbb{R}^L$ is a constant offset. Given a training set of length N , the linear inversion problem can be defined by

$$\mathbf{Y} = \mathbf{X}W^{\text{out}} + \mathbf{1}_N \mathbf{b}^\top, \quad (21)$$

where $\mathbf{Y} \in \mathbb{R}^{N \times L}$, $\mathbf{X} \in \mathbb{R}^{N \times N_r}$, and $\mathbf{1}_N := (1, \dots, 1)^\top \in \mathbb{R}^N$. We use Tikhonov regularization, finding the following ridge regression solution:

$$\hat{W}^{\text{out}} = (\mathbf{X}^\top \mathbf{A}_N \mathbf{X} + \lambda \mathbf{I}_{N_r})^{-1} \mathbf{X}^\top \mathbf{A}_N \mathbf{Y}, \quad \hat{\mathbf{b}}^\top = \frac{1}{N} \mathbf{1}_N^\top (\mathbf{Y} - \mathbf{X} \hat{W}^{\text{out}}), \quad (22)$$

where $\mathbf{I}_{N_r} \in \mathbb{R}^{N_r \times N_r}$ is the identity matrix, $\mathbf{A}_N := \mathbf{I}_N - \mathbf{1}_N \mathbf{1}_N^\top / N$, and $\lambda > 0$ is the regularization hyperparameter.

Dataset

Our target tasks are low-dimensional chaotic dynamical systems from the `dysts` database^{7,45}. Introduced in 2021, this library standardizes the chaotic systems that are frequently used for benchmarking time series forecasting methods. The database contains data, equations, and dynamic properties for more than 100 chaotic systems with strange attractors from various scientific disciplines.

To simplify the optimization of hyperparameters of the TN model, we follow the approach of 59 and select 70 systems where the ODEs have polynomial nonlinearities with degree no more than four. Also, the phase space dimension of these chaotic systems are either $P = 3$ or $P = 4$. Trajectories are generated with a slightly modified version of the code of reference 59. We generate two trajectories of 11000 points for each dynamical system (or task). The first trajectory is used for training and validation, while the second is for training and testing. We split each trajectory into three pieces: $N_{\text{warmup}} = 1000$ points for washing out the initial conditions of the ESN model (which we discard for the TN model so we train and evaluate over the same data), $N_{\text{train}} = 5000$ points for training, and $N_{\text{val}} = 5000$ points for validation (or testing). To test the performance, the models are run autonomously; after training, the outputs are fed back as inputs to predict the next time step. Also, the dynamical systems are integrated with 100 points per period of the time series, and we standardize each trajectory.

Validation

We divide the training and validation sets into 5000 points each, such that they are large enough to explore the whole attractor for all tasks and to guarantee the condition of persistently exciting input $N > R$ for training (Maximum value is $R = 4845$, for $M = D = P = 4$). For the TN model, we will explore the following values of maximum delay and maximum monomial degree: $M = \{1, 2, 3, 4\}$ and $D = \{2, 3, 4\}$. For validation of the ESN model, we fix the number of neurons to $N_r = 500$, and we select the following ranges of values: $\rho \in [0.8, 1.2]$, $g \in [0.1, 1]$, $\varepsilon \in [0.1, 1]$, $\lambda \in [10^{-13}, 10^{-1}]$.

We perform optimization as a grid search and only use a single trajectory for validation. Other approaches could potentially be explored, such as Bayesian optimization²⁰. Please note that the optimized hyperparameters may differ for newly generated trajectories, as these represent different tasks. Although cross-validation could mitigate the dependence of the optimal hyperparameters on the trajectory, we restrict ourselves to a single trajectory due to the computational cost of optimizing the ESN: the TN model takes approximately one hour with two threads, while the ESN takes over 60 hours. We also emphasize that one could still perform a more exhaustive exploration of the ESN hyperparameter space. However, we expect that since ESN models can be approximated by truncated Volterra series, we could always find a TN model that performs as well as the ESN while requiring a much simpler hyperparameter exploration.

For validation, we use the Wasserstein distance, which measures the similarity between two probability distributions, here the spectra of two temporal series. For one-dimensional signals, it is known⁶⁰ that the Wasserstein p -distance ($p \geq 1$) is given by the following integral:

$$W_p(\Phi_1, \Phi_2) = \int_0^1 |F_1^{-1}(x) - F_2^{-1}(x)|^p dx, \quad (23)$$

where Φ_1, Φ_2 are the probability distributions and F_1^{-1}, F_2^{-1} are the inverses of the cumulative distributions of Φ_1 and Φ_2 , respectively. Numerically, we calculate W_2 (for $p = 2$) with the function `WelchOptimalTransportDistance` from the

library `SpectralDistances.jl`⁶⁰. It computes the distance between two spectra estimated using a traditional spectral-estimation technique, the Welch method. Our final validation metric is the average of this distance over all the phase space variables. The hyperparameters with the lowest value of the Wasserstein metric are selected for testing.

Test metrics

For testing the models, we will evaluate two different aspects: their short-term memory and long-term memory (or climate) forecasting capabilities. To quantify the short-term prediction capabilities, we will first use the symmetric mean absolute percentage error (sMAPE)⁷:

$$\text{sMAPE}(n) = \frac{200}{n} \sum_{j=1}^n \frac{\|\mathbf{y}(j) - \hat{\mathbf{y}}(j)\|_2}{\|\mathbf{y}(j)\|_2 + \|\hat{\mathbf{y}}(j)\|_2}, \quad (24)$$

where $\mathbf{y}(j)$ and $\hat{\mathbf{y}}(j)$ are prediction and target respectively. It scales the absolute percentage error based on the magnitude of the two input time series. We take as the time index n the corresponding time of a Lyapunov exponent Λ for each task, such that we quantify the error to predict a single Lyapunov timescale unit, Λ^{-1} .

To quantify how many Lyapunov times the models can predict, we compute the valid prediction time (VPT) as in 61:

$$\text{VPT} = \Lambda \Delta t \left(\min_{N_{\text{ini}} < n \leq N_{\text{ini}} + N_{\text{pred}}} \left\{ n \mid \frac{\|\mathbf{y}(n) - \hat{\mathbf{y}}(n)\|_2}{\bar{E}} > \delta \right\} - N_{\text{ini}} - 1 \right), \quad (25)$$

where N_{ini} is the number of warmup inputs to resynchronize the trained model, Δt is the integration time step of the task, δ is the valid time error threshold, and \bar{E} is the average distance between target states computed from the initial training and warming up data as the mean of $\|\hat{\mathbf{y}}(j) - \hat{\mathbf{y}}(k)\|$ over $1 \leq j < k \leq N_{\text{warmup}} + N_{\text{train}}$ to normalize. We take $\delta = 0.2$, which represents a 20% error in the prediction, and we define $N_{\text{pred}} = 4000$, which is large enough for all tasks.

Both short-term memory metrics were averaged over 100 different initial conditions. These initial conditions are obtained by displacing the initial point of the test set evenly while warming up the models with $N_{\text{ini}} = 1000$ previous points, erasing the initial conditions, and resynchronizing the ESN model. Testing windows are taken long enough to compute these metrics for all tasks.

For long-term memory, we compute the Wasserstein distance as we did for validation, obtaining the difference between the target and predicted spectra. We used $N_{\text{test}} = 5000$ testing points with no average over different initial conditions. To compute all the testing metrics, we train the models over a new trajectory with the optimized hyperparameters, using the same division of $N_{\text{warmup}} = 1000$ points for warming up and $N_{\text{train}} = 5000$ points for training.

Results

The prediction capabilities of the TN model are demonstrated with the test metrics. All numerical computations were done on a laptop with 16 GB of RAM and an Intel Core i7-13620H CPU. The code is available at https://github.com/RMPhys/tnrc_paper.

Figure 1 shows the metrics for each of the 70 target tasks. The blue dots represent the values of the optimized TN models, while the yellow triangles represent the predictions of the optimized ESN models. The first and second rows contain the error bars of the average over 100 initial conditions. As can be observed, the TN model performs better than the ESN model for almost all tasks.

For the short-term memory metrics, the TN model shows a clear improvement for the first half of the tasks, while the second half displays a closer performance, especially for the Sprott family. We also observe a tendency of anticorrelation between sMAPE and VPT for both models: longer Lyapunov time predictability translates into smaller sMAPE errors for a single Lyapunov time.

Regarding the long-term memory (or climate) metric, we observe a more uniform profile between models, but the TN model keeps performing better for most of tasks. Indeed, there are several cases where the TN model outperforms the ESN model, reaching values of the metric smaller than 10^{-6} , while there are only a few tasks where the ESN beats the TN model.

Notice that some tasks show a strong correlation between all the metrics for both tasks, like HenonHelies and HyperRossler, while there are instances where correlations between all the metrics appear for only one of the models. For example, NoseHoover shows bad metrics for the ESN model, but the sMAPE metric is much worse than the other metrics for the TN model. The absence of correlations for some cases indicates that the different metrics must be assessed independently to conclude the models' various prediction capabilities.

Next, we compare the distribution of training times for both models with the optimized hyperparameters. Figure 2 displays a histogram where the x -axis is the CPU training time for one thread in seconds, while the y -axis represents the number of tasks.

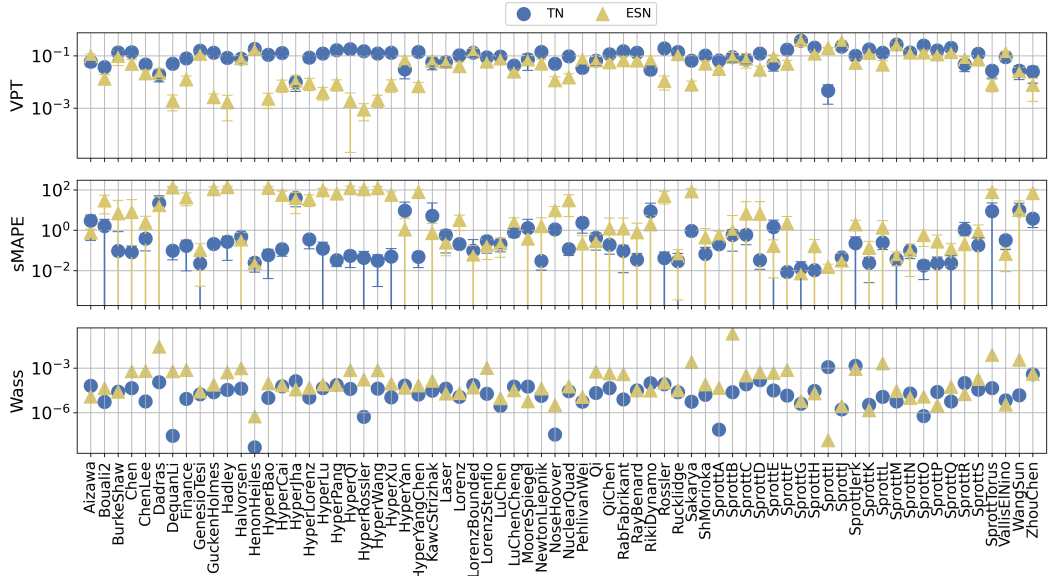


Figure 1. Comparison of the VPT and sMAPE and Wasserstein metrics for the TN and ESN models.

The blue and yellow columns correspond to the TN and ESN models. While the ESN models have a very narrow distribution, the TN models occupy a wider range of times due to the scaling of the TN algorithm with D and M . However, we find that the TN models can outperform the ESN models with at least one order of magnitude less training time.

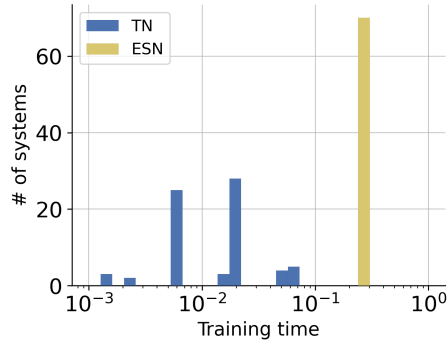


Figure 2. Histogram of CPU training times in seconds for the optimized hyperparameters.

Discussion

Chaotic time series prediction is one of the most popular applications of RC architectures, but the selection and optimization of RC models is an open problem. In this work, we explore a TN model introduced by Batselier^{34,35} that provides a low-rank approximation of the truncated Volterra series. Our goal is to provide a proof-of-concept for the suitability of TN models for time series prediction and, in particular, for learning chaotic systems. Our target tasks are a set of 70 standardized chaotic systems with polynomial nonlinearity, which serve as a perfect testbed. We benchmark the results of the TN model with an ESN model with a leak rate, having a fair comparison with one of the most extended models for chaotic time series prediction. We have shown two short-term memory metrics and one climate metric to provide an indicator of the forecasting capacity of the TN model. We obtained a better performance than the explored ESN model for most tasks with at least one order of magnitude smaller training time. This, together with only two hyperparameters to optimize, makes the TN model very attractive for large-scale scientific and industrial applications.

This work is a first step in the exploration of TN models as state-space systems for learning chaotic systems, and as such,

there is plenty of room for further exploration. A first step can be generalizing the TN implementation to predict complex spatiotemporal dynamics. Due to spatial discretization, the number of input features for these types of problems is usually of the order of hundreds or thousands of features, which, together with the need for a large number of training samples, demands a lot of computational resources for the SVD computation. A solution to this problem could be to compute a low-rank approximation of the randomized SVD⁶². Another important research direction is an exhaustive comparison with the state-of-the-art models that populate the time series and RC literature, like Volterra and polynomial kernels^{4,5} and SINDy^{59,63}. To understand when each model can stand out, a systematic comparison must be carried out. Due to the scaling of their algorithms' time complexity, the number of training points and input features would define the suitability of each method. In principle, kernel methods are preferred for problems with many input features but not many data points, while state-space models should operate more efficiently for a few features and long datasets. Complex spatiotemporal tasks would be a promising benchmark because they require a large number of training points and input features.

Appendix: Minimal-norm and symmetric solution of \mathbf{H}

Consider \mathbf{U} an $N \times I^D$ matrix whose rows represent the vectorization of D th-order symmetric tensors $\mathcal{U}_n \in \mathbb{R}^{I \times \dots \times I}$ for $n = 1, \dots, N$, that is,

$$\mathbf{U}(n, :) = \text{vec}(\mathcal{U}_n), \quad (26)$$

where the symbol $(:)$ represents the whole range of index values. In this manuscript in particular, $\mathbf{U}(n, :) = \mathbf{u}_n^D$. Then, each row of \mathbf{U} belongs to the vector space \mathcal{S}_D of vectorized symmetric tensors of order D in $\mathbb{R}^{I \times \dots \times I}$, defined as

$$\mathcal{S}_D = \{\mathbf{x} \in \mathbb{R}^{I^D} \mid \mathbf{x} = \text{vec}(\mathcal{X}), \mathcal{X} \in \text{Sym}_D(\mathbb{R})\}. \quad (27)$$

Since every row $\mathbf{U}(n, :)$ lies in \mathcal{S}_D , the row space $\mathcal{R}(\mathbf{U})$, which is the span of all the rows $\mathbf{U}(n, :)$, is a subspace of \mathcal{S}_D , that is, $\mathcal{R}(\mathbf{U}) \subset \mathcal{S}_D$, and any linear combination of the rows of \mathbf{U} is a vectorization of a symmetric tensor.

Let us now evaluate the minimal-norm solution of Eq. (11). Consider a target matrix $\mathbf{Y} \in \mathbb{R}^{N \times L}$, the solution $\mathbf{H} \in \mathbb{R}^{I^D \times L}$ is given by the Moore–Penrose pseudoinverse:

$$\mathbf{H} = \mathbf{U}^+ \mathbf{Y} = \mathbf{U}^\top \left(\mathbf{U} \mathbf{U}^\top \right)^+ \mathbf{Y} = \mathbf{U}^\top \mathbf{B}, \quad (28)$$

where we used the identity $\mathbf{U}^+ = \mathbf{U}^\top (\mathbf{U} \mathbf{U}^\top)^+$ and defined the matrix factor $\mathbf{B} := (\mathbf{U} \mathbf{U}^\top)^+ \mathbf{Y}$. Now we can see in Eq. (28) that each column of \mathbf{H} is formed as a linear combination of the columns of \mathbf{U}^\top , i.e. $\mathbf{H}(:, l) = \mathbf{U}^\top \mathbf{B}(:, l)$ for $l = 1, \dots, L$. This corresponds to a linear combination of the rows of \mathbf{U} when taking the transpose:

$$\mathbf{H}(:, l)^\top = \mathbf{B}(:, l)^\top \mathbf{U} = \sum_{n=1}^N \mathbf{B}(n, l) \mathbf{U}(n, :). \quad (29)$$

Therefore, $\mathbf{H}(:, l)^\top \in \mathcal{R}(\mathbf{U}) \subset \mathcal{S}_D$. A very important detail is that we did not make any assumptions about the rank of \mathbf{U} , nor about the sizes of N or R . Even if $\text{rank}(\mathbf{U}) < \min(N, R)$, the above discussion holds true. However, numerical computations are a different story.

Next, we construct two examples to show the deviations from theory that numerical experiments reveal regarding the symmetry of \mathbf{H} . The first case is based on constructing \mathbf{U} with random uncorrelated unidimensional inputs given by a uniform distribution $[0, 1]$. In this way, we ensure $\text{rank}(\mathbf{U}) = \min(N, R)$. The second case is based on constructing \mathbf{U} with highly correlated inputs given by the unidimensional sinusoidal signal

$$u(n) = \frac{1}{2} \left(1 + \sin \left(2\pi n \frac{2.11}{100} \right) \sin \left(2\pi n \frac{3.73}{100} \right) \sin \left(2\pi n \frac{4.11}{100} \right) \right), \quad (30)$$

such that $\text{rank}(\mathbf{U}) < \min(N, R)$. Now we fix the hyperparameters $M = D = 4$ and define a target for a simple task: we choose the memory task of recalling the last input, $\hat{y}(n) = u(n-1)$, and solve Eq. (11) by directly computing the pseudoinverse of \mathbf{U} with the function `pinv()` of *Julia*. To check the symmetry of a D th-order tensor $\mathcal{H} \in \mathbb{R}^{I \times \dots \times I}$, we compute the Euclidean distance between this tensor and all its permutations $\widehat{\mathcal{H}}_l$, for $l = 1, \dots, D!$, where $\widehat{\mathcal{H}}_l(j_1, \dots, j_D) = \mathcal{H}(\pi_l(i_1, \dots, i_D))$. The symmetry metric is then defined as

$$S = \sum_{l=1}^{D!} \|\mathcal{H} - \widehat{\mathcal{H}}_l\|. \quad (31)$$

Input	N	R	$\text{rank}(\mathbf{U})$	$\text{rank}(\mathbf{U}\mathbf{U}^\top)$	S
Uncorr.	50	70	50	50	1.37×10^{-11}
Corr.	50	70	48	41	0.13
Uncorr.	100	70	70	70	8.80×10^{-12}
Corr.	100	70	70	52	0.10

Table 1. Numerical values of rank and S for correlated and uncorrelated inputs.

Table 1 shows the values of S for the single column of \mathbf{H} together with the rank of \mathbf{U} , which is measured with the function `rank()` of *Julia* for both \mathbf{U} and $\mathbf{U}\mathbf{U}^\top$. We can make two observations about these results. First, we notice that for uncorrelated inputs, where $\text{rank}(\mathbf{U}) = \min(N, R)$, the mathematical condition $\text{rank}(\mathbf{U}) = \text{rank}(\mathbf{U}\mathbf{U}^\top)$ is fulfilled, while for correlated inputs, where $\text{rank}(\mathbf{U}) < \min(N, R)$, different values of $\text{rank}(\mathbf{U})$ and $\text{rank}(\mathbf{U}\mathbf{U}^\top)$ are obtained. Then, there is a problem in the numerical computation of the function `rank()` for correlated inputs. The second observation is that uncorrelated inputs yield a favorable symmetry metric ($S \sim 0$), while correlated inputs break the symmetry of \mathbf{H} . The latter happens despite the fact that, theoretically, the columns of \mathbf{H} must be symmetric independently of how \mathbf{U} is generated. Since we compute \mathbf{H} through the pseudoinverse \mathbf{U}^+ , the issue must be related to the numerical computation of `pinv()`.

To understand these numerical deviations, we display the singular values of \mathbf{U} and $\mathbf{U}\mathbf{U}^\top$ from Table 1 in Fig. 3. There we observe that uncorrelated inputs (blue and red lines) produce singular values with a clear cutoff, while correlated inputs (magenta and cyan lines) generate a smooth slope in the magnitude of the singular values. Therefore, establishing a threshold for the truncation of singular values seems a harder problem for the case of generating \mathbf{U} with correlated data.

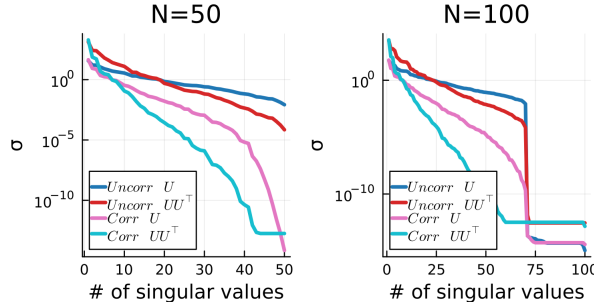


Figure 3. Singular values of \mathbf{U} for $N = 50, 100$ for $P = 1, M = 4$ and $D = 4$ when given random uncorrelated inputs (blue) and correlated data (red) from the example of Table 1.

Indeed, the threshold problem explains our previous observations. Both the pseudoinverse computation and the rank estimation of \mathbf{U} are based on the SVD computation and the truncation of the smaller singular values. As Eq. (18) shows, the pseudoinverse is constructed by inverting the diagonal matrix of singular values, and those singular values that are very close to zero need to be removed to ensure the numerical stability of the computation. Then, the SVD computation for \mathbf{U}^+ is much more stable for uncorrelated inputs than for correlated inputs, what is translated to the computation of S . The same idea applies to the deviations between $\text{rank}(\mathbf{U})$ and $\text{rank}(\mathbf{U}\mathbf{U}^\top)$, where the smoother behaviour of the singular values of \mathbf{U} and $\mathbf{U}\mathbf{U}^\top$ yield discrepancies when setting a numerical threshold.

In summary, the symmetry of the columns of \mathbf{H} is well preserved under $\text{rank}(\mathbf{U}) = \min(N, R)$, while the case $\text{rank}(\mathbf{U}) < \min(N, R)$ can break this symmetry because of numerical instabilities. In fact, careful attention must be paid to numerical experiments related to the SVD computation. Decisions like the choice of programming language can produce different results, since different languages use different criteria to truncate the singular values.

In this paper, we found that some of the chaotic tasks fulfill $\text{rank}(\mathbf{U}) < \min(N, R)$ due to the correlations between inputs at different time steps. In those cases, the functions `rank(U)` and `rank(UU^\top)` return different estimations, and we found a clear correlation: the higher is the discrepancy between estimations, the higher is S . See the notebook `test_symmetry.ipynb` in the source code for the details.

Data and code availability

Our data and code is available via the following link: https://github.com/RMPhys/tnrc_paper

References

1. Slingo, J. & Palmer, T. Uncertainty in weather and climate prediction. *Philos. Transactions Royal Soc. A: Math. Phys. Eng. Sci.* **369**, 4751–4767 (2011).
2. May, R. & McLean, A. R. *Theoretical ecology: principles and applications* (Oxford University Press, 2007).
3. Argyris, A. *et al.* Chaos-based communications at high bit rates using commercial fibre-optic links. *Nature* **438**, 343–346 (2005).
4. Gonon, L., Grigoryeva, L. & Ortega, J.-P. Reservoir kernels and volterra series. *arXiv preprint arXiv:2212.14641* (2022).
5. Grigoryeva, L., Ting, H. L. J. & Ortega, J.-P. Infinite-dimensional next-generation reservoir computing. *arXiv preprint arXiv:2412.09800* (2024).
6. Vlachas, P. R., Byeon, W., Wan, Z. Y., Sapsis, T. P. & Koumoutsakos, P. Data-driven forecasting of high-dimensional chaotic systems with long short-term memory networks. *Proc. Royal Soc. A: Math. Phys. Eng. Sci.* **474**, 20170844 (2018).
7. Gilpin, W. Model scale versus domain knowledge in statistical forecasting of chaotic systems. *Phys. Rev. Res.* **5**, 043252 (2023).
8. Pathak, J., Hunt, B., Girvan, M., Lu, Z. & Ott, E. Model-free prediction of large spatiotemporally chaotic systems from data: A reservoir computing approach. *Phys. review letters* **120**, 024102 (2018).
9. Griffith, A., Pomerance, A. & Gauthier, D. J. Forecasting chaotic systems with very low connectivity reservoir computers. *Chaos: An Interdiscip. J. Nonlinear Sci.* **29** (2019).
10. Vlachas, P.-R. *et al.* Backpropagation algorithms and reservoir computing in recurrent neural networks for the forecasting of complex spatiotemporal dynamics. *Neural Networks* **126**, 191–217 (2020).
11. Grigoryeva, L., Hart, A. & Ortega, J.-P. Chaos on compact manifolds: Differentiable synchronizations beyond the takens theorem. *Phys. Rev. E* **103**, 062204 (2021).
12. Grigoryeva, L., Hart, A. & Ortega, J.-P. Learning strange attractors with reservoir systems. *Nonlinearity* **36**, 4674 (2023).
13. Grigoryeva, L. & Ortega, J.-P. Universal discrete-time reservoir computers with stochastic inputs and linear readouts using non-homogeneous state-affine systems. *J. Mach. Learn. Res.* **19**, 1–40 (2018).
14. Grigoryeva, L. & Ortega, J.-P. Echo state networks are universal. *Neural Networks* **108**, 495–508 (2018).
15. Gonon, L. & Ortega, J.-P. Reservoir computing universality with stochastic inputs. *IEEE transactions on neural networks learning systems* **31**, 100–112 (2019).
16. Gonon, L. & Ortega, J.-P. Fading memory echo state networks are universal. *Neural Networks* **138**, 10–13 (2021).
17. Jaeger, H. *Tutorial on training recurrent neural networks, covering BPPT, RTRL, EKF and the echo state network approach*, vol. 5 (Citeseer, 2002).
18. Lukoševičius, M. & Jaeger, H. Reservoir computing approaches to recurrent neural network training. *Comput. science review* **3**, 127–149 (2009).
19. Sun, C. *et al.* A systematic review of echo state networks from design to application. *IEEE Transactions on Artif. Intell.* **5**, 23–37 (2022).
20. Platt, J. A., Penny, S. G., Smith, T. A., Chen, T.-C. & Abarbanel, H. D. A systematic exploration of reservoir computing for forecasting complex spatiotemporal dynamics. *Neural Networks* **153**, 530–552 (2022).
21. Gonon, L., Grigoryeva, L. & Ortega, J.-P. Approximation bounds for random neural networks and reservoir systems. *The Annals Appl. Probab.* **33**, 28–69 (2023).
22. Tanaka, G. *et al.* Recent advances in physical reservoir computing: A review. *Neural Networks* **115**, 100–123 (2019).
23. Nakajima, K. Physical reservoir computing—an introductory perspective. *Jpn. J. Appl. Phys.* **59**, 060501 (2020).
24. Nakajima, K. & Fischer, I. *Reservoir computing* (Springer, 2021).
25. Yan, M. *et al.* Emerging opportunities and challenges for the future of reservoir computing. *Nat. Commun.* **15**, 2056 (2024).
26. Gauthier, D. J., Bollt, E., Griffith, A. & Barbosa, W. A. Next generation reservoir computing. *Nat. communications* **12**, 1–8 (2021).
27. Barbosa, W. A. & Gauthier, D. J. Learning spatiotemporal chaos using next-generation reservoir computing. *Chaos: An Interdiscip. J. Nonlinear Sci.* **32** (2022).

28. Gauthier, D. J., Fischer, I. & Röhm, A. Learning unseen coexisting attractors. *Chaos: An Interdiscip. J. Nonlinear Sci.* **32** (2022).
29. Kent, R. M., Barbosa, W. A. & Gauthier, D. J. Controlling chaotic maps using next-generation reservoir computing. *Chaos: An Interdiscip. J. Nonlinear Sci.* **34** (2024).
30. Kent, R. M., Barbosa, W. A. & Gauthier, D. J. Controlling chaos using edge computing hardware. *Nat. Commun.* **15**, 3886 (2024).
31. Boyd, S. & Chua, L. Fading memory and the problem of approximating nonlinear operators with volterra series. *IEEE Transactions on circuits systems* **32**, 1150–1161 (1985).
32. Grigoryeva, L. & Ortega, J.-P. Differentiable reservoir computing. *J. Mach. Learn. Res.* **20**, 1–62 (2019).
33. Batselier, K., Chen, Z. & Wong, N. Tensor network alternating linear scheme for mimo volterra system identification. *Automatica* **84**, 26–35 (2017).
34. Batselier, K. Enforcing symmetry in tensor network mimo volterra identification. *IFAC-PapersOnLine* **54**, 469–474 (2021).
35. Batselier, K. A khatri-rao product tensor network for efficient symmetric mimo volterra identification. *IFAC-PapersOnLine* **56**, 7282–7287 (2023).
36. Khouaja, A. & Favier, G. Identification of parafac-volterra cubic models using an alternating recursive least squares algorithm. In *2004 12th European Signal Processing Conference*, 1903–1906 (IEEE, 2004).
37. Favier, G. & Bouilloc, T. Parametric complexity reduction of volterra models using tensor decompositions. In *2009 17th European Signal Processing Conference*, 2288–2292 (IEEE, 2009).
38. Favier, G. & Kibangou, A. Tensor-based approaches for nonlinear and multilinear systems modeling and identification. *Algorithms* **16**, 443 (2023).
39. Orús, R. Tensor networks for complex quantum systems. *Nat. Rev. Phys.* **1**, 538–550 (2019).
40. Bañuls, M. C. Tensor network algorithms: A route map. *Annu. Rev. Condens. Matter Phys.* **14**, 173–191 (2023).
41. Stoudenmire, E. & Schwab, D. J. Supervised learning with tensor networks. *Adv. neural information processing systems* **29** (2016).
42. Cheng, S., Wang, L., Xiang, T. & Zhang, P. Tree tensor networks for generative modeling. *Phys. Rev. B* **99**, 155131 (2019).
43. Tomut, A. *et al.* Compactifai: extreme compression of large language models using quantum-inspired tensor networks. *arXiv preprint arXiv:2401.14109* (2024).
44. Batselier, K. Low-rank tensor decompositions for nonlinear system identification: A tutorial with examples. *IEEE Control. Syst. Mag.* **42**, 54–74 (2022).
45. Gilpin, W. Chaos as an interpretable benchmark for forecasting and data-driven modelling. *arXiv preprint arXiv:2110.05266* (2021).
46. Horn, R. A. & Johnson, C. R. *Matrix analysis* (Cambridge university press, 2012).
47. Kalman, D. A singularly valuable decomposition: the svd of a matrix. *The college mathematics journal* **27**, 2–23 (1996).
48. Oseledets, I. V. & Tyrtyshnikov, E. E. Breaking the curse of dimensionality, or how to use svd in many dimensions. *SIAM J. on Sci. Comput.* **31**, 3744–3759 (2009).
49. Kolda, T. G. & Bader, B. W. Tensor decompositions and applications. *SIAM review* **51**, 455–500 (2009).
50. Oseledets, I. V. Tensor-train decomposition. *SIAM J. on Sci. Comput.* **33**, 2295–2317 (2011).
51. Verstraete, F., Garcia-Ripoll, J. J. & Cirac, J. I. Matrix product density operators: Simulation of finite-temperature and dissipative systems. *Phys. review letters* **93**, 207204 (2004).
52. Zwolak, M. & Vidal, G. Mixed-state dynamics in one-dimensional quantum lattice systems: A time-dependent superoperator renormalization algorithm. *Phys. review letters* **93**, 207205 (2004).
53. Oseledets, I. V. Approximation of $2^d \times 2^d$ matrices using tensor decomposition. *SIAM J. on Matrix Analysis Appl.* **31**, 2130–2145 (2010).
54. Batselier, K., Ko, C.-Y. & Wong, N. Tensor network subspace identification of polynomial state space models. *Automatica* **95**, 187–196 (2018).
55. Favier, G., Kibangou, A. Y. & Bouilloc, T. Nonlinear system modeling and identification using volterra-parafac models. *Int. J. Adapt. Control. Signal Process.* **26**, 30–53 (2012).

56. Bouilloc, T. & Favier, G. Nonlinear channel modeling and identification using baseband volterra–parafac models. *Signal Process.* **92**, 1492–1498 (2012).
57. Memmel, E., Menzen, C. & Batselier, K. Bayesian framework for a mimo volterra tensor network. *IFAC-PapersOnLine* **56**, 7294–7299 (2023).
58. Jaeger, H. The “echo state” approach to analysing and training recurrent neural networks-with an erratum note. *Bonn, Ger. Ger. Natl. Res. Cent. for Inf. Technol. GMD Tech. Rep.* **148**, 13 (2001).
59. Kaptanoglu, A. A., Zhang, L., Nicolaou, Z. G., Fasel, U. & Brunton, S. L. Benchmarking sparse system identification with low-dimensional chaos. *Nonlinear Dyn.* **111**, 13143–13164 (2023).
60. Bagge Carlson, F. & Chitre, M. New metrics between rational spectra and their connection to optimal transport. *arXiv e-prints* arXiv–2004 (2020).
61. Wikner, A. *et al.* Stabilizing machine learning prediction of dynamics: Novel noise-inspired regularization tested with reservoir computing. *Neural Networks* **170**, 94–110 (2024).
62. Batselier, K., Yu, W., Daniel, L. & Wong, N. Computing low-rank approximations of large-scale matrices with the tensor network randomized svd. *SIAM J. on Matrix Analysis Appl.* **39**, 1221–1244 (2018).
63. Brunton, S. L., Proctor, J. L. & Kutz, J. N. Discovering governing equations from data by sparse identification of nonlinear dynamical systems. *Proc. national academy sciences* **113**, 3932–3937 (2016).

Acknowledgements

We thank Hannah Lim Jing Ting, Miguel C. Soriano, and Juan-Pablo Ortega for inspiring and useful discussions. We would like to thank Lyudmila Grigoryeva for their attentive reading and insightful comments on this manuscript. RMP acknowledges the QCDI project funded by the Spanish Government.

Author contributions

RMP and RO designed the research; RMP conducted the simulations and analyzed the results; both authors wrote and reviewed the manuscript.

Competing interests

The authors declare no competing interests.